

## Article

# Rodingites in the Darbut Ophiolitic Mélange, West Junggar: New Insights into Rodingitization and Tectonic Evolution

Pan Zhang <sup>1,\*</sup>, Guocan Wang <sup>2</sup>, Huaguo Liu <sup>1</sup> and Feng Li <sup>1</sup><sup>1</sup> China Earthquake Disaster Prevention Center, Beijing 100029, China<sup>2</sup> School of Earth Sciences, China University of Geosciences, Wuhan 430074, China

\* Correspondence: pzhang@cug.edu.cn

**Abstract:** The Darbut ophiolitic mélange is located in the central West Junggar area, southwestern Central Asian Orogenic Belt (CAOB), and rodingites are widespread within serpentinized peridotites in the mélange. Here, we conducted field, structural, mineralogical, and geochemical investigations of the Darbut rodingites for the first time to constrain their metasomatic processes. Rodingites usually occur as strongly sheared blocks surrounded by chloritic blackwall, and their preferred axial surface orientations are subparallel to the serpentinite foliations. Based on the petrology and geochemistry of these metasomatic rocks, two stages of metasomatic processes, namely rodingitization and derodingitization, were recognized: (1) rodingitization of gabbroic protolith was characterized by the input of Ca and the release of Si, K, Na, and LILE; this stage was related to the diapiric emplacement of the Darbut ophiolitic mélange in the Late Carboniferous; and (2) derodingitization of rodingites led to the replacement of Ca-rich minerals by chlorite, accompanied by Mg increase, and depletions of Ca and REE; the derodingitization stage occurred under enhanced CO<sub>2</sub>/H<sub>2</sub>O ratio conditions and was likely associated with regional postcollision volcanism in the Early Permian. Hence, the rodingite in the Darbut ophiolitic mélange provides important fingerprints recording the tectonic evolution.

**Keywords:** rodingite; ophiolitic mélange; metasomatic processes; tectonic evolution



**Citation:** Zhang, P.; Wang, G.; Liu, H.; Li, F. Rodingites in the Darbut Ophiolitic Mélange, West Junggar: New Insights into Rodingitization and Tectonic Evolution. *Minerals* **2022**, *12*, 1229. <https://doi.org/10.3390/min12101229>

Academic Editor: Federica Zaccarini

Received: 20 September 2022

Accepted: 26 September 2022

Published: 28 September 2022

**Publisher's Note:** MDPI stays neutral with regard to jurisdictional claims in published maps and institutional affiliations.



**Copyright:** © 2022 by the authors. Licensee MDPI, Basel, Switzerland. This article is an open access article distributed under the terms and conditions of the Creative Commons Attribution (CC BY) license (<https://creativecommons.org/licenses/by/4.0/>).

## 1. Introduction

The term rodingite was first introduced by [1] to describe altered gabbros in the Dun Mountain serpentinites, New Zealand. In a general sense, rodingites are considered to represent “Ca-rich and Si-undersaturated rocks formed by metasomatic alteration of mainly mafic rocks” [2–8]. They usually occur as boudins or dykes surrounded by serpentinites or serpentinized peridotites in ophiolitic mélanges and are mainly composed of Ca–Al and Ca–Mg silicates, such as garnet, secondary clinopyroxene, prehnite, epidote, clinozoisite, and vesuvianite (e.g., [9–11]).

Given that rodingites are spatially associated with serpentinites, rodingitization is often thought to occur along with serpentinization on the ocean floor (e.g., [2,3,12,13]), and rodingites have been present in cores drilled into the ocean floor [14]. However, it has also been documented that the rodingitization may occur during subduction at prograde to peak metamorphic conditions (e.g., [5,9,15,16]) or during exhumation and retrograde metamorphism (e.g., [6,15,17,18]). Therefore, a greater understanding of rodingitization can help elucidate element migration and fluid–rock interaction [19,20] and distinguish different geological processes [21,22].

The Darbut ophiolitic mélange in the West Junggar Orogen is characterized by variably sized ultramafic to mafic rocks and cherts, and they usually display as tectonic blocks included in a foliated serpentinite matrix [23]. Several studies have focused on the geochronology and geochemistry of mafic rocks to reveal their petrogenesis and geodynamic setting and to reconstruct the tectonic evolution of the West Junggar orogen [24–26]. However, little attention has been paid on the rodingites exposed in the Darbut ophiolitic

mélange. The Darbut rodingites are well-preserved and widespread and mainly associated with serpentinized peridotites, which provides an ideal opportunity to study the petrogenesis of rodingites. In this study, we first presented field and petrological observations, and geochemical compositions of rodingites collected from the Darbut ophiolitic mélangé, in order to study the rodingitization processes and its geological significance.

## 2. Geological Background and Field Geology

### 2.1. Tectonic Framework of West Junggar

The West Junggar Orogen is located in the southwestern part of the Central Asian Orogenic Belt (CAOB) (Figure 1a), which is one of the largest Phanerozoic accretionary orogens [27–29]. It has undergone a prolonged and complicated tectonic evolution, accompanied by formation, subduction, accretion, and closure of the paleo-Junggar Ocean during the Paleozoic [23,26,28,30–36], a major branch of the Paleo-Asian Ocean. Although there is no general consensus on the tectonic division of the West Junggar orogen [23,26,34,37], a popular division suggests that West Junggar can be divided into the northern, central, and southern tectonic units [23,38] (Figure 1b), which obviously recorded different evolutionary processes.

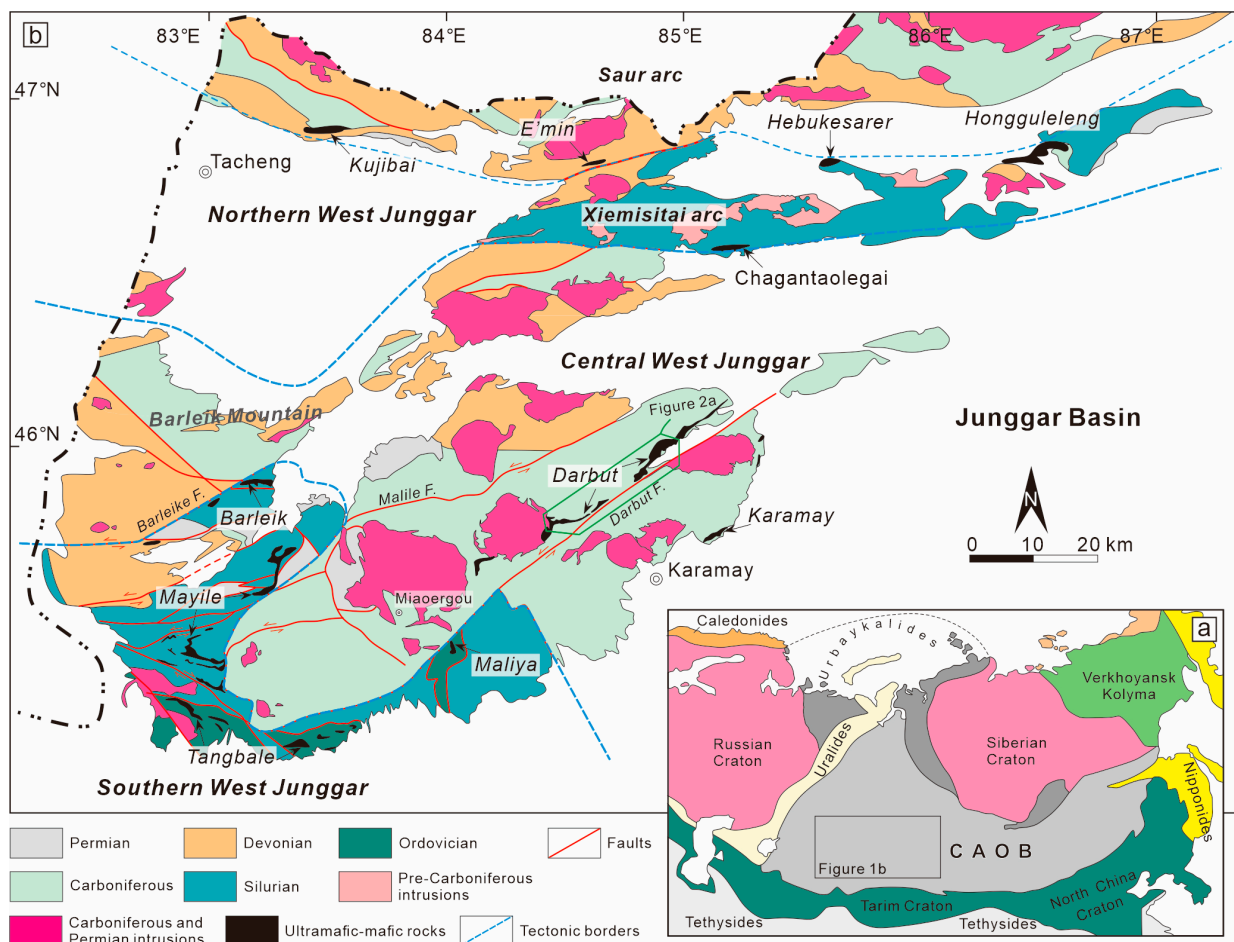


**Figure 1.** (a) Tectonic framework of Central Asian Orogenic Belt (CAOB) (modified from [27]); (b) simplified geological map showing geotectonic divisions of West Junggar Orogen (modified from [28]).

Northern West Junggar contains two E–W-striking intraoceanic arcs: the Late Paleozoic Sawuer arc in the north and Early Paleozoic Xiemisitai arc in the south [39–41]; the boundary between these two arcs is marked by the Kujibai–Hongguleleng ophiolitic mélangé belt [35,42]. The Sawuer arc mainly includes Devonian to Carboniferous volcanic–sedimentary rocks and

minor Ordovician volcanic rocks that are intruded by Carboniferous granitoids. The Xiemisitai arc comprises Silurian volcanic rocks and Late Ordovician to Early Devonian granitoids, which has been considered as the eastern extension of the Boshchekul–Chingiz arc. Southern West Junggar is composed of ophiolitic mélanges, arc-related magmatic rocks, volcano-sedimentary sequences, and high-pressure metamorphic rocks [28,31,42,43]. They represent an Early Paleozoic intraoceanic arc–trench system, which has been collided to the north margin of the Paleo-Kazakhstan Continent prior to the Early Devonian [28,43].

Central West Junggar is separated from the northern West Junggar domain by the Chagantaolegai suture zone that contains Cambrian ophiolitic rocks with a mid-ocean ridge feature [44]. This domain is dominated by Devonian to Carboniferous volcanoclastic sedimentary rocks and two Late Paleozoic ophiolitic mélanges (named as the Darbut ophiolitic mélange in the north and Karamay ophiolitic mélange in the south) [23,26,32,34], intruded by Late Carboniferous–Early Permian magmatic rocks [45–47]. The Carboniferous volcanoclastic succession displays coherent turbidite sequences deposited during the Viséan to Moscovian [28]. They are subdivided into Xibeikulasi, Baogutu, Tailegula, and Hala’alate formations from the bottom to top [48] and are dominantly composed of tuffaceous sandstone, tuff, and tuffaceous siltstone. The Darbut and Karamay ophiolitic mélanges occur as northeast-trending discontinuous chaotic units, and they have high-angle right-lateral fault contacts with the Carboniferous sequences [23]. The Late Carboniferous–Early Permian magmatic rocks mainly consist of A- and I-type granitoids, adakites, and high-Mg mafic dikes related to postcollision [47] or ridge subduction [46].

## 2.2. Brief Summary of the Darbut Ophiolitic Mélange

The Darbut ophiolitic mélange, situated along the northern side of the Darbut Fault (Figure 2b), is a significant unit to study the subduction and accretion processes of the Junggar Ocean. It is characterized by a typical “block-in-matrix” structure; tectonic blocks, mainly including serpentized peridotite, gabbro, rodingite, basalt, pillow lava, chert, and sandstone, are surrounded by strong foliated serpentines (Figures 2a and 3a). Geochronological data suggest that the gabbro and basalt of the Darbut ophiolitic mélange mainly formed in the Devonian [24,25]. Three generations of structures were recognized by [23] and involved thrust-imbricated deformation ( $D_1$ ), NE–SW-striking right-lateral shear zones ( $D_2$ ), and NE–SW-striking transcurrent left-lateral strike-slip faults ( $D_3$ ).  $D_1$  is locally observed in some outcrops and likely associated with early-stage accretion of oceanic crust, the  $D_2$  structures are interpreted to represent the emplacement of the ophiolitic mélange, and  $D_3$  is related to regional postcollisional deformation [23].

## 2.3. Field Relationships of the Rodingites

Rodingites are spatially associated with the serpentized peridotite and mainly exposed in the western segment of the Darbut ophiolitic mélange. Geological mapping shows the structural relationships (Figure 2b). Serpentinites are highly sheared, with strong foliations. In general, the foliation planes steeply dip to northwest with an average altitude of 315/82 (Figure 2a). The individual blocks of rodingites are surrounded by the serpentinite foliations (Figure 3f–j). Rodingites are gray-white and vary in size, ranging from several decimeters to several meters in length. They are generally ellipsoidal, and some change to elongate, suggesting strong sheared deformation (Figure 3f,g,j). The axial surfaces of the rodingite blocks have a preferred northwest–southeast orientation and are subparallel to the serpentinite foliations (Figure 3f–j). Rodingitization decreases from the rim to the core of the blocks, and some of the large blocks preserve relatively fresh gabbro in their cores (Figure 3b–e). A reaction zone usually developed between the rodingite and serpentinite (serpentinized peridotite) (Figure 3b–i). The reaction zones are black and have sharp contacts with them, forming a “blackwall” wrapped around the rodingite. Blackwalls are usually several decimeters in thickness; in most cases, they are not deformed or foliated (Figure 3b–i).



aggregates of anhedral. Blackwalls are dominated by chlorite; grossular, diopside, and magnetite often present in the form of fine-grained aggregates of anhedral with the chloritic matrix (Figure 4c,d).

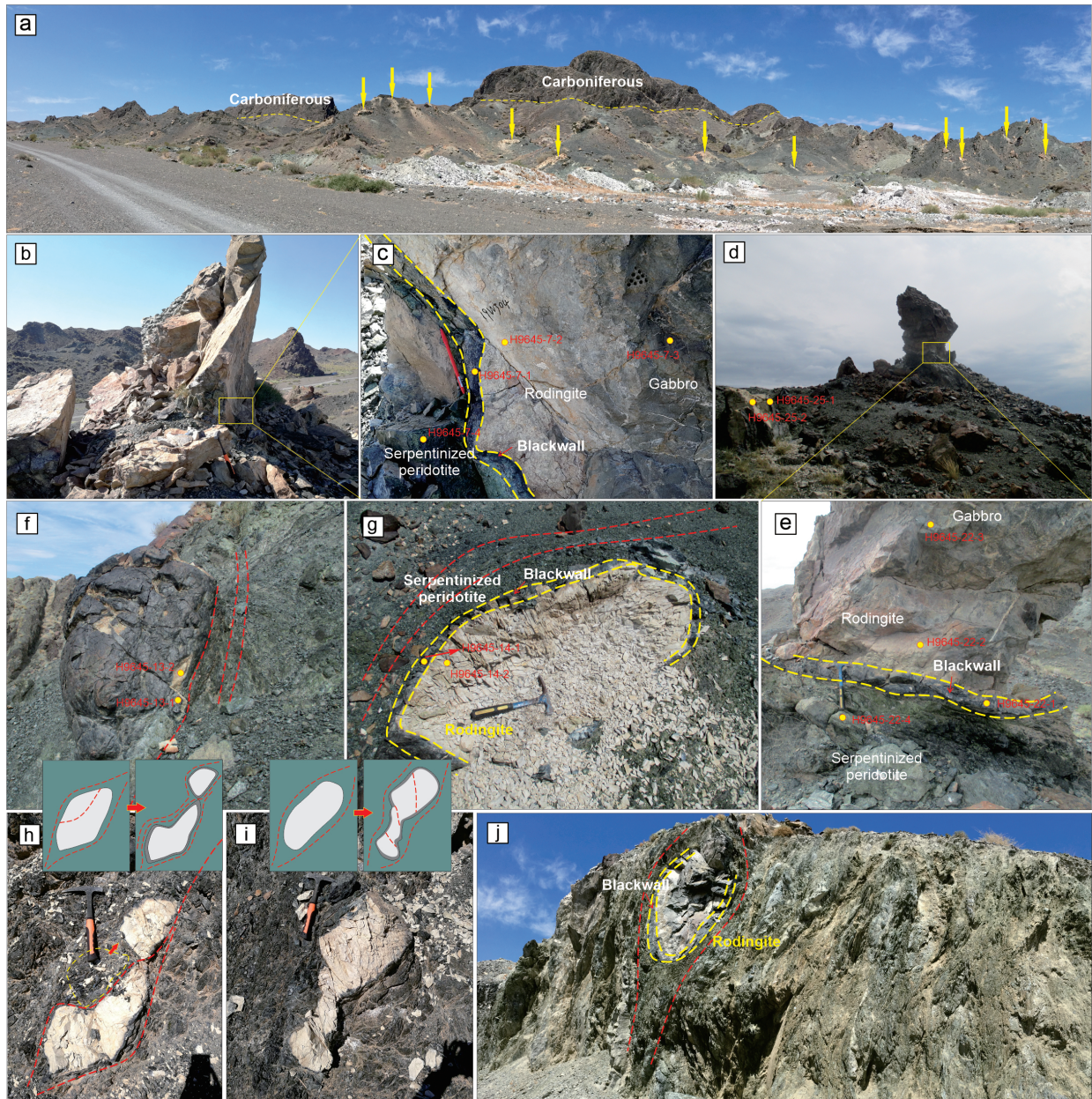


**Figure 3.** Field photographs showing field relationship of rodingites in ophiolitic mélangé. (a) Outcrop of Darbut ophiolitic mélangé (yellow arrows indicate rodingite blocks); (b–j), and (j) rodingite blocks within foliated serpentinite matrix; reaction zones (blackwalls) usually developed between rodingite and serpentinite (yellow circles indicate sample locations in this study; red dotted lines indicate foliation of serpentinite; yellow dotted lines indicate boundary of blackwalls); (h,i) rodingite blocks were offset by small shearing faults and surrounded by unbroken blackwall (cartoons show evolution of rodingite blocks).

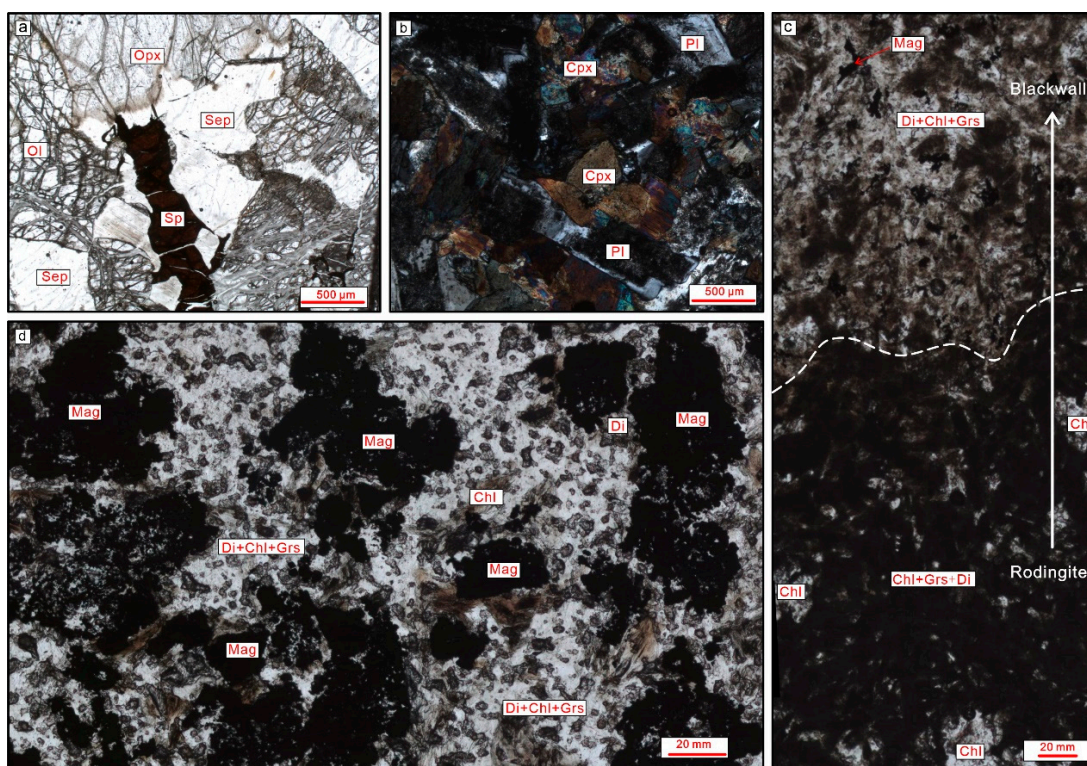


**Figure 4.** Photomicrographs showing mineral compositions and textures of rocks in Darbut ophiolitic mélange. (a) Serpentinized peridotite with Opx, Ol, Sep, and Sp; (b) gabbro with Opx and Pl; (c) contact zone of rodingite and blackwall; blackwall mainly consists of Chl, Grs, Di, and Mag; rodingite mainly consists of Grs, Di, and Chl; (d) blackwall with Chl, Di, Grs, and Mag. Abbreviations for different minerals: Opx—orthopyroxene; Ol—olivine; Sep—serpentine; Sp—spinel; Pl—plagioclase; Chl—chlorite; Grs—grossular; Di—diopside; and Mag—magnetite.

### 3. Geochemistry

#### 3.1. Analytical Methods

Samples for whole-rock major- and trace-element analyses were crushed, and fresh chips were selected and washed in purified water. The cleaned chips were then powdered in an agate mortar to less than 200 meshes. Major- and trace-element measurements were carried out at the State Key Laboratory of Geological Processes and Mineral Resources (GPMR), at CUG. Major oxides were analyzed using an X-ray fluorescence spectrometer, with analytical precision better than 5%. Loss on ignition was measured after heating to 1000 °C. Trace elements were determined by inductively coupled plasma–mass spectrometry (ICP-MS) using an Agilent 7700e system, with analytical precision better than 5%. Detailed sample-digestion and analytical procedures for trace-element analyses are the same as described by [51].

#### 3.2. Results

Fifteen samples, including six pairs of adjacent rodingites and blackwalls and three fresh gabbros, were analyzed for whole-rock major- and trace-element concentrations. The analytical results are listed in Table 1.

**Table 1.** Whole-rock analyses of selected samples from Darbut ophiolitic mélange.

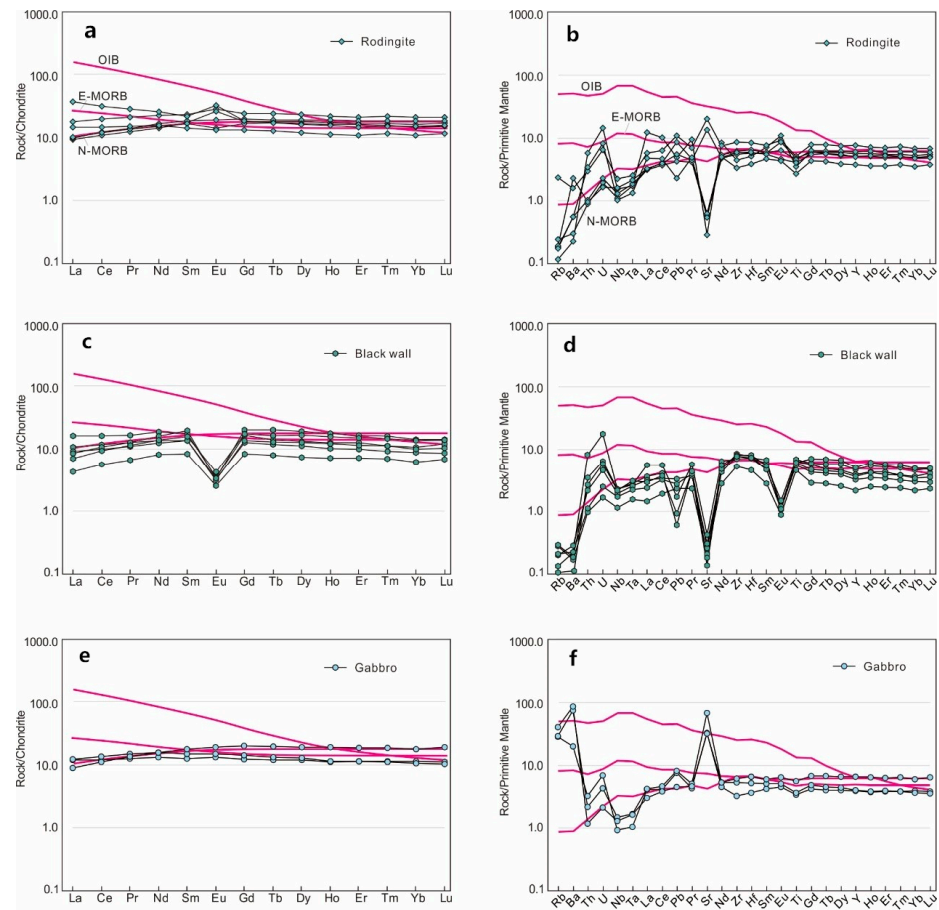
Sample Rock Type	H9645-7-2 Rodingite	H9645-7-1 Blackwall	H9645-22-2 Rodingite	H9645-22-1 Blackwall	H9645-25-2 Rodingite	H9645-25-1 Blackwall	H9645-14-2 Rodingite
SiO <sub>2</sub>	39.80	30.30	43.60	27.55	36.99	31.01	35.45
TiO <sub>2</sub>	0.59	1.29	0.87	3.04	0.98	1.48	1.02
Al <sub>2</sub> O <sub>3</sub>	12.03	14.75	14.05	14.63	14.23	13.66	12.44
Fe <sub>2</sub> O <sub>3</sub>	9.42	14.69	8.58	21.85	9.57	12.35	13.01
MnO	0.17	0.55	0.15	1.28	0.20	0.95	0.42
MgO	5.14	26.62	7.61	21.22	6.29	28.29	14.49
CaO	29.85	0.32	21.36	0.98	27.99	0.27	16.87
Na <sub>2</sub> O	0.04	0.04	0.18	0.01	0.06	0.02	0.04
K <sub>2</sub> O	0.01	0.00	0.01	0.00	0.01	0.00	0.02
P <sub>2</sub> O <sub>5</sub>	0.10	0.11	0.09	0.20	0.11	0.10	0.09
LOI	2.06	10.80	3.27	9.26	3.37	11.40	5.76
SUM	99.22	99.48	99.76	100.00	99.79	99.53	99.60
Li	3.99	10.3	19.3	18.2	6.63	13.3	18.6
Be	0.26	0.011	0.37	0.017	0.29	0.017	0.13
Sc	31.9	37.5	32.8	49.0	35.3	28.8	48.8
V	294	386	217	600	293	352	321
Cr	14.0	263	264	119	40.4	53.1	297
Co	31.0	80.2	37.3	101	31.8	84.9	51.9
Ni	19.5	114	96.3	90.7	30.5	40.9	98.8
Cu	74.9	5.10	36.3	151	55.6	5.33	24.7
Zn	58.6	97.3	57.5	116	69.9	122	96.1
Ga	10.0	5.72	11.1	6.63	12.2	6.72	4.65
Rb	0.11	0.18	0.12	0.11	0.12	0.13	0.15
Sr	11.5	3.82	285	21.7	13.3	2.90	12.2
Y	16.9	22.8	23.0	58.8	27.2	21.3	25.6
Zr	37.6	85.2	66.4	196	69.6	89.7	60.7
Nb	0.74	1.54	1.15	2.85	0.92	1.20	0.79
Sn	0.32	0.030	0.56	0.18	0.62	0.055	0.16
Cs	0.010	0.016	0.039	0.062	0.10	0.060	0.13
Ba	3.93	1.29	16.1	1.60	3.87	1.57	2.12
La	3.29	2.02	2.24	3.77	2.18	1.62	2.15
Ce	8.33	6.45	6.94	14.5	7.13	5.64	6.56
Pr	1.34	1.20	1.23	2.92	1.27	1.08	1.14
Nd	6.83	7.34	6.66	17.2	7.27	6.48	6.48
Sm	2.07	2.94	2.42	6.60	2.63	2.37	2.53
Eu	0.73	0.18	0.79	0.77	1.05	0.25	1.45
Gd	2.57	4.12	3.26	8.58	3.79	3.52	3.53
Tb	0.45	0.74	0.60	1.57	0.67	0.60	0.63
Dy	2.84	4.87	4.04	10.6	4.58	4.12	4.38
Ho	0.59	0.99	0.86	2.23	1.00	0.88	0.92
Er	1.70	2.70	2.49	6.28	2.86	2.47	2.61
Tm	0.28	0.41	0.38	0.98	0.45	0.37	0.41
Yb	1.74	2.39	2.34	5.80	2.94	2.26	2.60
Lu	0.28	0.36	0.36	0.88	0.44	0.35	0.41
Hf	1.18	2.27	1.80	5.40	2.02	2.45	1.79
Ta	0.054	0.12	0.088	0.20	0.077	0.090	0.070
Tl	0.0049	0.0058	0.0048	0.0058	0.0047	0.0027	0.0052
Pb	0.16	0.065	0.39	0.094	0.61	0.19	0.30
Th	0.29	0.23	0.081	0.33	0.087	0.093	0.076
U	0.17	0.12	0.035	0.18	0.049	0.052	0.041

Table 1. Cont.

Sample	H9645-14-1	H9645-13-2	H9645-13-1	H9645-12-2	H9645-12-1	H9645-7-3	H9645-22-3	H9645-20
Rock Type	Blackwall	Rodingite	Blackwall	Rodingite	Blackwall	Fresh Gabbro	Fresh Gabbro	Fresh Gabbro
SiO <sub>2</sub>	30.98	43.84	31.54	31.30	29.27	48.18	48.74	50.88
TiO <sub>2</sub>	0.98	1.12	1.26	0.76	1.36	1.21	0.79	0.74
Al <sub>2</sub> O <sub>3</sub>	14.60	12.91	13.78	14.15	14.33	15.33	15.90	15.23
Fe <sub>2</sub> O <sub>3</sub>	13.48	10.85	11.73	16.28	19.01	10.95	7.96	10.17
MnO	0.51	0.16	0.81	0.59	0.79	0.18	0.14	0.17
MgO	27.13	4.00	28.79	11.38	24.30	7.13	7.94	5.92
CaO	0.23	23.51	0.27	17.97	0.39	9.73	11.97	9.15
Na <sub>2</sub> O	0.02	0.25	0.02	0.04	0.01	3.54	3.13	4.44
K <sub>2</sub> O	0.00	0.06	0.00	0.01	0.00	1.23	0.62	1.13
P <sub>2</sub> O <sub>5</sub>	0.07	0.15	0.10	0.15	0.17	0.10	0.10	0.09
LOI	11.12	2.46	11.37	6.40	10.17	2.18	2.76	1.36
SUM	99.12	99.30	99.67	99.02	99.79	99.76	100.05	99.28
Li	27.7	7.48	15.9	9.06	7.99	28.6	25.7	12.0
Be	0.0091	0.46	0.017	0.12	0.0055	0.28	0.29	0.23
Sc	21.9	25.7	23.2	50.4	43.3	43.4	39.3	41.0
V	262	274	330	407	594	304	184	324
Cr	270	2.94	55.9	27.6	47.1	158	138	153
Co	87.5	32.5	96.1	54.9	120	41.6	31.4	30.3
Ni	190	9.56	65.3	27.2	55.0	49.7	63.7	57.9
Cu	6.41	53.8	3.44	24.0	45.0	35.6	97.9	112
Zn	106	84.8	122	126	104	77.5	53.5	75.0
Ga	5.63	14.7	5.21	4.96	10.1	14.3	13.3	15.2
Rb	0.18	1.49	0.13	0.075	0.085	25.9	18.4	18.2
Sr	4.35	420	6.43	6.12	8.95	671	1448	700
Y	9.79	34.3	16.2	23.0	17.4	29.9	18.6	18.1
Zr	58.5	96.3	85.2	50.2	77.9	69.1	60.6	36.3
Nb	0.82	1.61	1.36	1.11	1.59	0.93	1.07	0.67
Sn	0.053	0.78	0.053	0.23	0.040	0.44	0.71	0.28
Cs	0.15	0.15	0.014	0.021	0.022	1.26	0.96	1.09
Ba	1.17	11.1	1.97	1.61	1.52	604	523	139
La	0.99	3.97	2.15	8.30	3.78	2.10	2.91	2.82
Ce	3.41	11.2	5.94	18.0	9.76	6.78	8.32	7.30
Pr	0.63	1.89	1.01	2.57	1.54	1.27	1.41	1.20
Nd	3.71	10.1	5.68	11.3	8.64	7.34	7.28	6.14
Sm	1.24	3.41	2.06	3.13	2.60	2.70	2.29	1.89
Eu	0.15	1.56	0.18	1.80	0.20	1.10	0.85	0.76
Gd	1.67	4.66	2.76	3.57	3.39	4.08	2.90	2.49
Tb	0.30	0.84	0.48	0.61	0.52	0.74	0.50	0.44
Dy	1.86	5.53	3.14	3.84	3.33	4.85	3.24	3.00
Ho	0.41	1.17	0.68	0.85	0.70	1.07	0.63	0.62
Er	1.16	3.32	1.87	2.32	2.06	3.05	1.88	1.86
Tm	0.17	0.53	0.28	0.37	0.28	0.47	0.28	0.29
Yb	1.04	3.38	1.67	2.39	1.77	2.98	1.80	1.94
Lu	0.17	0.51	0.26	0.38	0.30	0.48	0.26	0.28
Hf	1.40	2.57	2.17	1.57	2.18	2.02	1.61	1.13
Ta	0.063	0.10	0.10	0.071	0.11	0.068	0.069	0.044
Tl	0.0044	0.016	0.010	0.0048	0.0034	0.14	0.13	0.10
Pb	0.16	0.78	0.23	0.34	0.12	0.32	0.59	0.54
Th	0.081	0.25	0.18	0.49	0.69	0.10	0.19	0.28
U	0.035	0.14	0.096	0.31	0.37	0.045	0.090	0.15

*Fresh Gabbros:* Fresh gabbros have small variations of SiO<sub>2</sub> (48.18–50.88 wt.%), Al<sub>2</sub>O<sub>3</sub> (15.23–15.90 wt.%), and total alkalis (Na<sub>2</sub>O + K<sub>2</sub>O = 3.75–5.57 wt.%) and have low TiO<sub>2</sub> (0.74–1.21 wt.%) and moderate CaO (9.15–11.97 wt.%) contents. The MgO contents range from 5.92 to 7.94 wt.%, and the FeOT contents vary from 7.17 to 9.86 wt.%, with the

Mg number ranging from 54 to 66 (calculated as  $\text{Mg}/(\text{Mg} + \text{Fe})$  in molecular). On the chondrite-normalized diagram (Figure 5e), they show slightly depleted LREE patterns ( $\text{La}/\text{Sm}_{\text{cn}} = 0.50\text{--}0.96$ ;  $\text{La}/\text{Yb}_{\text{cn}} = 0.50\text{--}1.16$ ; cn—chondrite normalized) with no Eu anomalies ( $\text{Eu}/\text{Eu}^* = 1.01\text{--}1.07$ ). On the primitive mantle-normalized diagram (Figure 5f), all samples display anomalies of negative high-field-strength elements (HFSEs such as Th, Nb, Ta, and Ti) and positive large-ion lithophile elements (LILEs such as Rb, Ba, and Sr).



**Figure 5.** Chondrite- and primitive mantle-normalized diagrams for studied samples. Normalization values from [52]. N-MORB—normal-MORB; E-MORB—enriched-MORB; OIB—ocean island basalt.

**Rodingites:** Rodingites are characterized by low  $\text{SiO}_2$  (31.30–43.84 wt.%) and total alkalis ( $\text{Na}_2\text{O} + \text{K}_2\text{O} = 0.05\text{--}0.31$  wt.%) and significantly high CaO (16.87–29.85 wt.%). They have moderate variations in  $\text{TiO}_2$  (0.59–1.12 wt.%),  $\text{Al}_2\text{O}_3$  (12.03–14.23 wt.%), MgO (4.00–14.49 wt.%), and FeO (8.58–14.65 wt.%), with the Mg number ranging from 42 to 69. On the chondrite-normalized diagram (Figure 5a), they are characterized by slightly depleted to enrichment in LREE ( $\text{La}/\text{Sm}_{\text{cn}} = 0.55\text{--}1.71$ ;  $\text{La}/\text{Yb}_{\text{cn}} = 0.53\text{--}2.49$ ) without marked Eu anomalies ( $\text{Eu}/\text{Eu}^* = 0.86\text{--}1.65$ ). On the primitive mantle-normalized diagram (Figure 5b), they display negative Nb, Ta, and Ti anomalies with variable Sr anomalies ( $\text{Sr}/\text{Sr}^* = 0.03\text{--}2.89$ ).

**Blackwalls:** Blackwalls are characterized by low contents of  $\text{SiO}_2$  (29.27–31.54 wt.%), CaO (0.23–0.39 wt.%), and total alkalis ( $\text{Na}_2\text{O} + \text{K}_2\text{O} = 0.01\text{--}0.04$  wt.%). They possess high contents of MgO (24.30–29.54 wt.%) and FeO (9.44–17.11 wt.%) with the Mg number ranging from 72 to 85. On the chondrite-normalized diagram (Figure 5c), they show slightly depleted LREE patterns ( $\text{La}/\text{Sm}_{\text{cn}} = 0.44\text{--}0.94$ ;  $\text{La}/\text{Yb}_{\text{cn}} = 0.51\text{--}1.53$ ), with significantly negative Eu anomalies ( $\text{Eu}/\text{Eu}^* = 0.16\text{--}0.31$ ). On the primitive mantle-normalized diagram (Figure 5d), they display anomalies of negative large-ion lithophile elements (LILEs such as Rb, Ba, and Sr) and slightly negative Nb and Ta anomalies.

### 3.3. Isocon Analysis

Isocon analysis has been widely used to determine chemical gains and losses during mass transfer (e.g., [10,18]). According to [53], the immobile elements should lie on a straight line (isocon), and the slope of the isocon represents the overall change in mass relative to protolith. Elements plotting above the immobility isocon are added into the rock during mineralization and alteration. Elements plotting below the immobility isocon are removed from the rock. In this study, we relatively compared rodingites and blackwalls with fresh gabbros using this method to estimate the compositional variations. Al, Zr, and Ti are usually considered as immobile elements during metasomatism [54]. In this study, Zr and Ti were utilized to generate immobility isocon because of their high positive correlations among each other.

The isocon line for rodingites has a slope of 1.15, indicating an average mass loss of about 13%. Most major elements in rodingites were variably mobile (Figure 6a). There were slight increases in Mn and strong increases in Ca, whereas total alkalis (Na, K) and Si were obviously depleted. Fe, Mg, and P plot near the isocon line, which implies insignificant modification. Regarding the trace elements (Figure 6c), REEs, HFSEs (e.g., Nb, Ta, Th, U, and Hf), and V appear to be relatively immobile since they plot very close to the isocon line. In contrast, most LILEs (e.g., Rb, Ba, Sr, and Pb) were extracted from the protolith during rodingitization. The isocon line for the blackwall has a slope of 1.78, indicating an average mass loss of about 44%. CaO, total alkalis (Na, K), and Si contents have been significantly depleted; Al, P, and Fe are also slightly decreased; while MgO and MnO are highly enriched (Figure 6d). For the trace elements (Figure 6e,f), HFSEs (e.g., Nb, Ta, Th, U, Hf) and V are relatively immobile; LILEs (e.g., Rb, Ba, Sr, and Pb) and REEs, especially Eu, display clear depletion.

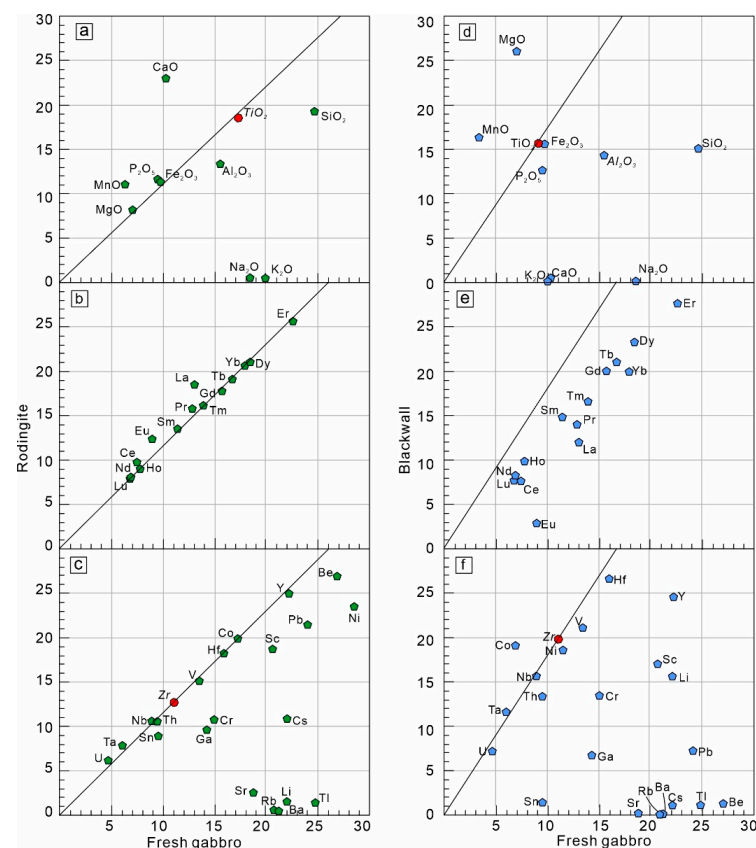


**Figure 6.** Isocon plots using method of [53]. Major elements plotted as wt.% of oxides, and trace elements in ppm. Solid lines represent constant Ti and Zr.

## 4. Discussions

### 4.1. Rodingite Protolith

Many geochronological, geochemical, and structural studies have been carried out to decipher the formation process of the Darbut ophiolitic mélange [23,26]. However, there has never been any attention about the rodingites that are widespread throughout the ophiolitic mélange. Recent studies have reached a consensus that rodingites were formed through metasomatism of mafic to felsic rocks [5–8]. In the Darbut ophiolitic mélange, rodingites exhibit geochemical compositions similar to the fresh gabbros, and they all plot in the basalt field on the Nb/Y–Zr/Ti diagram [55] (Figure 7a). Sometimes, gabbro relicts were preserved in the center of some large rodingite blocks. These lines of evidence indicate that gabbros should be the protolith of rodingites. The author of [3] suggested that blackwalls associated with rodingites formed from the meta-peridotite by the metasomatic addition of aluminum. In this study, blackwalls were characterized by low contents of SiO<sub>2</sub> but high contents of MgO similar to the serpentinized peridotite. However, they plot in the basalt field on the Nb/Y–Zr/Ti diagram (Figure 7a) and share very similar REE and HFSE patterns with fresh gabbros and rodingites. Thus, the protoliths of blackwalls were also gabbros rather than peridotites.

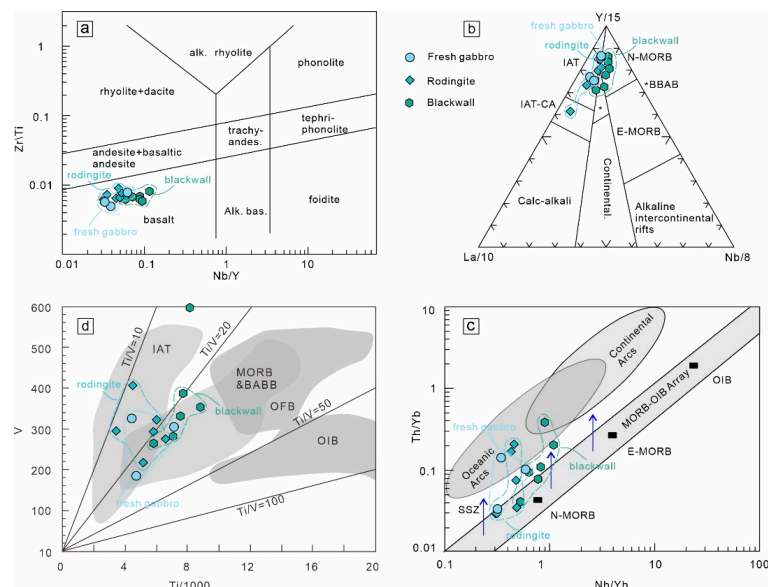


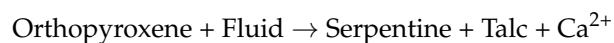
**Figure 7.** (a) Zr/Ti versus Nb/Y diagram adopted from [55]; (b) Y–La–Nb ternary discrimination diagram adopted from [56]; (c) Th/Yb versus Nb/Yb diagram adopted from [57]; (d) V–Ti diagram adopted from [58]. N-MORB—normal-MORB; E-MORB—enriched-MORB; OIB—ocean island basalt; IAT— island-arc tholeiite; BABB—back-arc basin basalt.

In this study, REEs, except Eu in blackwalls, and HFSEs (e.g., Th, Nb, Zr, and Ti) showed consistent distribution patterns on the chondrite- and primitive mantle-normalized diagrams (Figure 5), and isocron analysis documents limited mobility of these elements during rodingitization (Figure 6). Accordingly, these immobile elements can be used for interpreting the petrogenetic signatures of gabbroic protoliths. Fresh gabbros and rodingites are characterized by slightly depleted to enrichment LREE patterns on the chondrite-normalized diagram, which are indistinguishable from N-MORB patterns. However, they show slightly negative Nb and Ta anomalies on the primitive mantle-normalized diagram. On Y/15–Nb/8–La/10 (Figure 7b), they plot in the mix fields of IAT and MORB [56]. Most of them have low Ti/V ratios, also plotting in the mixed fields of IAT and MORB on the V–Ti diagram [58] (Figure 7d), and they have relatively high Th/Yb ratios, plotting in the MORB–OIB array to the subduction-related field on the Th/Yb–Nb/Yb diagram [57] (Figure 7c). These lines of evidence indicated that their magma source was influenced by subduction

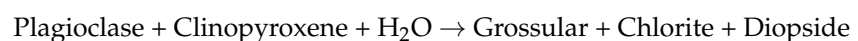
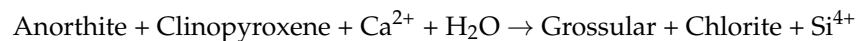
inputs [59,60]. Therefore, (meta-) gabbros were considered to have formed in a subduction-related tectonic setting. This conclusion is consistent with previous studies [23,26,28,36] that suggested that the Darbut ophiolite was formed in a back-arc ocean basin during the Devonian.

#### 4.2. Metasomatic Process and Element Mobility

Based on the above petrology and geochemistry of these metasomatic rocks, two stages of metasomatic processes, namely rodingitization and derodingitization, were recognized [18,61]. The first metasomatic stage (stage 1) corresponds to rodingitization processes. In all occurrences, rodingites are spatially associated with serpentinites and located at the juxtapositions of ultramafic and mafic rocks. Given the close proximity of the two rock types and their chemical contrasts, it has been assumed that rodingites form by the reaction with Ca released during the serpentinization of the ultramafic host rocks [7,20,62–64]. Generally, Ca-rich serpentinizing fluids are attributable to the breakdown of primary clinopyroxene during serpentinization [65]. However, in the Darbut ophiolitic mélange, ultramafic rocks mainly consist of harzburgite with only minor amounts of lherzolite [24,49,50]. Considering that orthopyroxene also contains small amounts of calcium, the dissolution of the orthopyroxene during serpentinization likely plays an important role in the formation of Ca-rich fluids in this study. The reactions describing the above are given through the following equations [65].

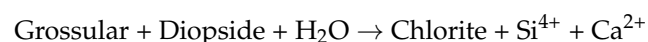


The mobilized Ca is transported from the serpentinite to the gabbro layers, where it leads to the crystallization of Ca-rich phases such as grossular and diopside and, hence, the formation of rodingites. It is evidently observed that rodingites are characterized by significant Ca enrichments. This stage can be described by the following mineral reactions [65]:



This process was accompanied by the release of Si, alkalis, and other fluid mobile elements, such as LILEs (e.g., Rb, Ba, Sr, and Pb), leading to the remarkable loss of these elements in rodingites. Therefore, the rodingitization process in the Darbut ophiolitic mélange was characterized by the input of Ca and the release of Si, K, Na, and LILEs.

The second metasomatic stage (stage 2) corresponds to derodingitization processes, forming the chlorite marginal zones (blackwalls). Derodingitization is commonly attributed to the breakdown of the previously formed rodingitization-related mineral phases. Grossular and diopside were consumed and replaced by chlorite, which can be explained by the following reaction [8].



The results of the isocon analysis indicated that most major and trace elements of blackwalls were modified during the derodingitization process [18,61]. The replacement of Ca-rich minerals by chlorite would have led to the Mg increase and Ca depletions. In addition, blackwalls display significant REE depletions compared with rodingites. Generally, REE mobilization is related to the composition of hydrous fluids; high water–rock ratios and CO<sub>2</sub>-fluid phases can promote the mobility of the REE [10,66,67].

#### 4.3. Implications for the Tectonic Setting

It has been assumed that rodingites can form in a wide temperature and pressure condition [14–18]. In the Darbut ophiolitic mélange, rodingites usually occur as sheared bodies

within the foliated serpentinites. Our geological mapping indicated that the preferred orientation of the axial surfaces of these rodingite blocks is subparallel to the serpentinite foliations, indicating a strong sheared deformation. In some cases, rodingite blocks were offset by small shear zones. The authors of [23] suggested that the Darbut ophiolitic mélangé was extruded into the Carboniferous strata through NE-striking subvertical right-lateral shear zones during the Late Carboniferous. Therefore, the rodingitization process was likely related to the diapiric emplacement of the Darbut ophiolitic mélangé. In contrast, the blackwalls around the rodingite bodies only suffered weathering without any sheared deformation. The above observation reflects the fact that blackwalls were generated after the diapiric emplacement of the Darbut ophiolitic mélangé. Listwaenites extensively outcrop in the Darbut ophiolitic mélangé and have been considered to be transformed by the reaction between serpentinite and CO<sub>2</sub>-rich fluid during the Early Permian (296–302 Ma) [49,68]. The inferred REE mobility of blackwalls also suggests a high water–rock ratio and high amounts of CO<sub>2</sub>. Thus, we suggested that the derodingitization process of rodingites may have occurred in this stage.

Finally, we attempted here to reconstruct the process of formation and evolution of the Darbut rodingite. In the Devonian, slab rollback of the Junggar Ocean formed a back-arc basin in the central West Junggar area, forming the SSZ-type Darbut ophiolite [26,36] (Figure 8a). In this setting, the gabbroic protoliths of rodingites were derived from a depleted mantle source that had been metasomatized by slab-derived fluids. The back-arc oceanic basin began to shrink and progressively evolved into a remnant oceanic basin in response to the successive bending of the Kazakhstan Orocline in the Early Carboniferous [23,30,32,69], and numerous volcanoclastic and tuffaceous materials derived from the Carboniferous arc-related rocks were quickly deposited in the remnant basin (Figure 8b). Regional convergence of the southwestern Altaids in the Late Carboniferous led to the extensive deformation in the central West Junggar area and to the tectonic extrusion of the Darbut ophiolitic mélangé accompanied by strong dismemberment and shearing of the previous SSZ-type ophiolite (Figure 8c) [23]. In this stage, the diapiric emplacement of the Darbut ophiolitic mélangé also resulted in the extensive serpentinization of ultramafic rocks, inducing the intensive rodingitization of gabbro blocks (Figure 8d). In the Early Permian, postcollision volcanism likely released a mass of metasomatic fluids with a high water–rock ratio and high CO<sub>2</sub> content [49,68], resulting in the derodingitization of rodingites (Figure 8d).

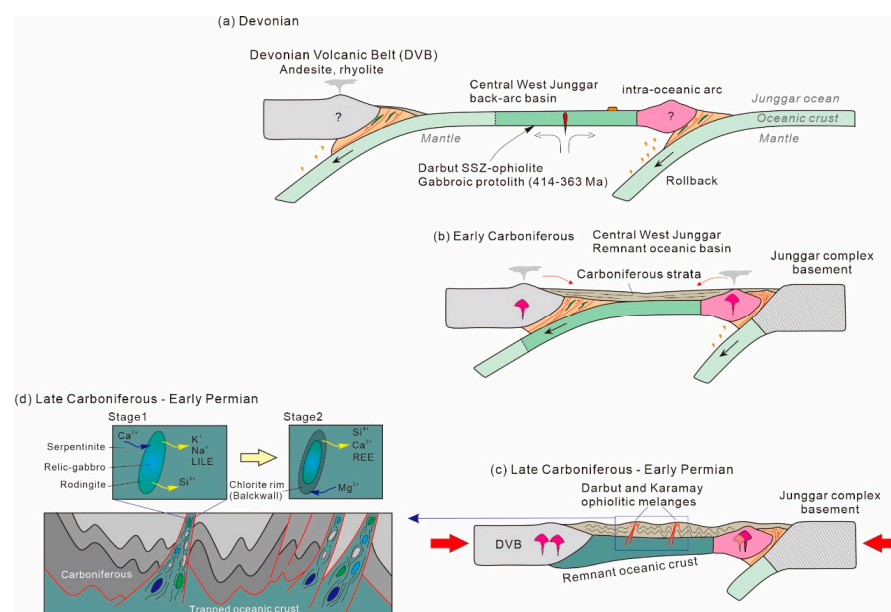


**Figure 8.** Geological model for geodynamic evolution of Darbut rodingite.

## 5. Conclusions

- (1) The protoliths of rodingites and blackwalls in the Darbut ophiolitic mélange are gabbros; they were derived from a depleted mantle source that had been metasomatized by slab-derived fluids.
- (2) Two stages of metasomatic processes (i.e., rodingitization and derodingitization) were recognized. Rodingitization of gabbroic protolith was characterized by the input of Ca and the release of Si, K, Na, and LILEs. Derodingitization of rodingites led to the replacement of Ca-rich minerals by chlorite and to the Mg increase and Ca and REE depletions.
- (3) The rodingitization process was related to the diapiric emplacement of the Darbut ophiolitic mélange in the Late Carboniferous; the derodingitization process occurred in the Early Permian and was likely associated with regional postcollision volcanism.

**Author Contributions:** Conceptualization, P.Z. and G.W.; methodology, P.Z.; software, P.Z.; validation, P.Z. and G.W.; formal analysis, P.Z.; investigation, P.Z. and G.W.; resources, P.Z. and G.W.; data curation, P.Z.; writing—original draft preparation, P.Z.; writing—review and editing, G.W., H.L. and F.L.; visualization, P.Z.; supervision, G.W.; project administration, P.Z. and G.W.; funding acquisition, P.Z. and G.W. All authors have read and agreed to the published version of the manuscript.

**Funding:** This study was supported by the National Natural Science Foundation of China (no. 42102263) via a grant to P. Zhang and the Urban Active Fault Detection and Seismic Risk Assessment Project of China Earthquake Administration (no. 14406033401).

**Data Availability Statement:** Not applicable.

**Acknowledgments:** We acknowledge the editor and two anonymous reviewers for their detailed and constructive comments that have resulted in significant improvements in the paper. We thank Jing Zhang, Dongan Zhao, and Huicheng Wen from China University of Geosciences (Wuhan) for helping with the field and laboratory work.

**Conflicts of Interest:** The authors declare no conflict of interest.

## References

1. Bell, J.M.; Clarke, E.C.; Marshall, P. *The Geology of the Sun Mountain Subdivision, Nelson*; New Zealand Geological Survey Bulletin 12 New Series; Mackay, Government Printer: Wellington, New Zealand, 1911.
2. Coleman, R.G. Serpentinities, rodingites, and tectonic inclusions in Alpine-type Mountain chains. *Geol. Soc. Am. Spec. Pap.* **1963**, *73*, 130–131.
3. Frost, B.R. Contact metamorphism of serpentinite, chloritic blackwall and rodingite at Paddy-Go-Easy Pass, Central Cascades, Washington. *J. Petrol.* **1975**, *16*, 272–313. [[CrossRef](#)]
4. O’Hanley, D.S.; Schandl, E.S.; Wicks, F.J. The origin of rodingites from Cassiar, British-Columbia, and their use to estimate T and P (H<sub>2</sub>O) during serpentinization. *Geochim. Cosmochim. Acta* **1992**, *56*, 97–108. [[CrossRef](#)]
5. Li, X.P.; Zhang, L.; Wei, C.; Ai, Y.; Chen, J. Petrology of rodingite derived from eclogite in western Tianshan, China. *J. Metamorph. Petrol.* **2007**, *25*, 363–382. [[CrossRef](#)]
6. Li, X.P.; Zhang, L.F.; Wilde, S.A.; Song, B.; Liu, X.M. Zircon from rodingite in the Western Tianshan serpentinite complex: Mineral chemistry and U-Pb ages define nature and timing of rodingitization. *Lithos* **2010**, *118*, 17–34. [[CrossRef](#)]
7. Bach, W.; Klein, F. The petrology of seafloor rodingites: Insights from geochemical reaction path modeling. *Lithos* **2009**, *112*, 103–117. [[CrossRef](#)]
8. Laborda-López, C.; López-Sánchez-Vizcaíno, V.; Marchesi, C.; Gómez-Pugnaire, M.T.; Garrido, C.J.; Jabaloy-Sánchez, A.; Padrón-Navarta, J.A.; Hidas, K. High-P metamorphism of rodingites during serpentinite dehydration (Cerro del Almiraz, Southern Spain): Implications for the redox state in subduction zones. *J. Metamorph. Geol.* **2018**, *36*, 1141–1173. [[CrossRef](#)]
9. Shen, T.T.; Wu, F.T.; Zhang, L.F.; Hermann, J.; Li, X.P.; Du, J.X. In-situ U-Pb dating and Nd isotopic analysis of perovskite from a rodingite blackwall associated with UHP serpentinite from southwestern. *Chem. Geol.* **2016**, *431*, 67–82. [[CrossRef](#)]
10. Tang, Y.; Zhai, Q.G.; Hu, P.Y.; Wang, J.; Xiao, X.C.; Wang, H.T.; Tang, S.H.; Lei, M. Rodingite from the Beila ophiolite in the Bangong–Nujiang suture zone, northern Tibet: New insights into the formation of ophiolite-related rodingite. *Lithos* **2018**, *316–317*, 33–47. [[CrossRef](#)]
11. Rogkala, A.; Petrounias, P.; Koutsovitis, P.; Giannakopoulou, P.P.; Pomonis, P.; Lampropoulou, P.; Hatzipanagiotou, K. Rodingites from the Veria-Naousa ophiolite (Greece): Mineralogical evolution, metasomatism and petrogenetic processes. *Geochemistry* **2022**, *82*, 125860. [[CrossRef](#)]

12. Schandl, E.S.; O'Hanley, D.S.; Wicks, F.J. Rodingites in serpentinized ultramafic rocks of the Abitibi Greenstone Belt, Ontario. *Can. Mineral.* **1989**, *27*, 579–591.
13. Schandl, E.S.; O'Hanley, D.S.; Wicks, F.J. Fluid inclusions in rodingite: A geothermometer for serpentinization. *Econ. Geol.* **1990**, *85*, 1273–1276. [[CrossRef](#)]
14. Frost, B.R.; Beard, J.S.; McCaig, A.; Condliffe, E. The formation of micro-rodingites from IODP Hole U1309D: Key to understanding the process of serpentinization. *J. Petrol.* **2008**, *49*, 1579–1588. [[CrossRef](#)]
15. Li, X.P.; Duan, W.Y.; Zhao, L.Q.; Schertl, H.P.; Kong, F.M.; Shi, T.Q.; Zhang, X. Rodingites from the Xigaze ophiolite, southern Tibet: New insights into the processes of rodingitization. *Eur. J. Mineral.* **2017**, *29*, 821–837. [[CrossRef](#)]
16. Tsikouras, B.; Karipi, S.; Rigopoulos, I.; Perraki, M.; Pomonis, P.; Hatzipanagiotou, K. Geochemical processes and petrogenetic evolution of rodingite dykes in the ophiolite complex of Othrys (Central Greece). *Lithos* **2009**, *113*, 540–554. [[CrossRef](#)]
17. Ferrando, S.; Frezzotti, M.L.; Orione, P.; Conte, R.C.; Compagnoni, R. Late-Alpine rodingitization in the Bellecombe meta-ophiolites (Aosta Valley, Italian Western Alps): Evidence from mineral assemblages and serpentinization-derived H<sub>2</sub>-bearing brine. *Int. Geol. Rev.* **2010**, *52*, 1220–1243. [[CrossRef](#)]
18. Koutsovitis, P.; Magganas, A.; Pomonis, P.; Ntaflos, T. Subduction-related rodingites from East Othris, Greece: Mineral reactions and physicochemical conditions of formation. *Lithos* **2013**, *172–173*, 139–157. [[CrossRef](#)]
19. Dai, J.G.; Wang, C.S.; Liu, S.A.; Zhu, D.C.; Ke, S. Deep carbon cycle recorded by calcium-silicate rocks (rodingites) in a subduction-related ophiolite. *Geophys. Res. Lett.* **2016**, *43*, 11635–11643. [[CrossRef](#)]
20. Gussone, N.; Austrheim, H.; Westhues, A.; Mezger, K. Origin of Rodingite Forming Fluids Constrained by Calcium and Strontium Isotope Ratios in the Leka Ophiolite Complex. *Chem. Geol.* **2020**, *542*, 119598. [[CrossRef](#)]
21. Mubarak, H.S.; Azer, M.K.; Surour, A.A.; Moussa, H.E.; Asimow, P.D.; Kabesh, M.M. Mineralogical and geochemical study of rodingites and associated serpentinized peridotite, Eastern Desert of Egypt, Arabian-Nubian Shield. *Lithos* **2020**, *374–375*, 105720. [[CrossRef](#)]
22. Duan, W.Y.; Li, X.P.; Schertl, H.P.; Willner, A.P.; Wang, S.J.; Chen, S.; Sun, G.M. Rodingitization records from ocean-floor to high pressure metamorphism in the Xigaze ophiolite 5720, southern Tibet. *Gondwana Res.* **2022**, *104*, 126–153. [[CrossRef](#)]
23. Zhang, P.; Wang, G.C.; Polat, A.; Zhu, C.Y.; Shen, T.Y.; Chen, Y.; Chen, C.; Guo, J.S.; Wu, G.L.; Liu, Y.T. Emplacement of the ophiolitic mélanges in the west Karamay area: Implications for the Late Paleozoic tectonic evolution of West Junggar, northwestern China. *Tectonophysics* **2018**, *747–748*, 259–280. [[CrossRef](#)]
24. Yang, G.X.; Li, Y.J.; Santosh, M.; Yang, B.K.; Yan, J.; Zhang, B.; Tong, L.L. Geochronology and geochemistry of basaltic rocks from the Sartuohai ophiolitic mélange, NW China: Implications for a Devonian mantle plume within the Junggar Ocean. *J. Asian Earth Sci.* **2012**, *59*, 141–155. [[CrossRef](#)]
25. Yang, G.X.; Li, Y.J.; Gu, P.Y.; Yang, B.K.; Tong, L.L.; Zhang, H.W. Geochronological and geochemical study of the Darbut Ophiolitic complex in the West Junggar (NW China): Implications for petrogenesis and tectonic evolution. *Gondwana Res.* **2012**, *21*, 1037–1049. [[CrossRef](#)]
26. Zhang, P.; Wang, G.C.; Polat, A.; Shen, T.Y.; Chen, Y.; Zhu, C.Y.; Wu, G.L. Geochemistry of mafic rocks and cherts in the Darbut and Karamay ophiolitic mélanges in West Junggar, northwestern China: Evidence for a Late Silurian to Devonian back-arc basin system. *Tectonophysics* **2018**, *745*, 395–411. [[CrossRef](#)]
27. Sengör, A.M.C.; Natal'in, B.A.; Sunal, G.; van der Voo, R. The tectonics of the Altaids: Crustal growth during the construction of the continental lithosphere of Central Asia between ~750 and ~130 Ma ago. *Annu. Rev. Earth Planet. Sci.* **2018**, *46*, 439–494. [[CrossRef](#)]
28. Zhang, P.; Wang, G.C.; Shen, T.Y.; Polat, A.; Zhu, C.Y. Paleozoic convergence processes in the southwestern Central Asian Orogenic Belt: Insights from U-Pb dating of detrital zircons from West Junggar, northwestern China. *Geosci. Front.* **2021**, *12*, 531–548. [[CrossRef](#)]
29. Şengör, A.M.C.; Natal'in, B.A.; Burtman, V.S. Evolution of the Altaid tectonic collage and Palaeozoic crustal growth in Eurasia. *Nature* **1993**, *364*, 299–307. [[CrossRef](#)]
30. Chen, S.; Pe-Piper, G.; Piper, D.J.W.; Guo, Z. Ophiolitic mélanges in crustal-scale fault zones: Implications for the Late Paleozoic tectonic evolution in West Junggar, China. *Tectonics* **2014**, *33*, 2419–2443. [[CrossRef](#)]
31. Ren, R.; Han, B.F.; Xu, Z.; Zhou, Y.Z.; Liu, B.; Zhang, L.; Chen, J.F.; Su, L.; Li, J.; Li, X.H.; et al. When did the subduction first initiate in the southern Paleo-Asian Ocean: New constraints from a Cambrian intra-oceanic arc system in West Junggar, NW China. *Earth Planet. Sci. Lett.* **2014**, *388*, 222–236. [[CrossRef](#)]
32. Liu, B.; Han, B.F.; Chen, J.F.; Ren, R.; Zheng, B.; Wang, Z.Z.; Feng, L.X. Closure time of the Junggar-Balkhash Ocean: Constraints from Late Paleozoic volcano-sedimentary sequences in the Barleik Mountains, West Junggar, NW China. *Tectonics* **2017**, *36*, 2823–2845. [[CrossRef](#)]
33. Choulet, F.; Faure, M.; Cluzel, D.; Chen, Y.; Lin, W.; Wang, B.; Jahn, B.M. Architecture and evolution of accretionary orogens in the Altaids collage: The early Paleozoic west junggar (NW China). *Am. J. Sci.* **2012**, *312*, 1098–1145. [[CrossRef](#)]
34. Choulet, F.; Faure, M.; Cluzel, D.; Chen, Y.; Lin, W.; Wang, B. From oblique accretion to transpression in the evolution of the Altaid collage: New insights from West Junggar, northwestern China. *Gondwana Res.* **2012**, *21*, 530–547. [[CrossRef](#)]
35. Yang, Y.Q.; Zhao, L.; Zheng, R.G.; Xu, Q.Q. Evolution of the early Paleozoic Hongguleleng-Balkybay Ocean: Evidence from the Hebukesaiyer ophiolitic mélange in the northern West Junggar, NW China. *Lithos* **2019**, *324–325*, 519–536. [[CrossRef](#)]

36. Zhang, P.; Wang, G.C.; Shen, T.Y.; Zhu, C.Y. Late Paleozoic back-arc basin in West Junggar (northwestern China): New geochronological and petrogenetic constraints from basalts and cherts in the western Karamay area. *J. Geodyn.* **2019**, *126*, 1–11. [[CrossRef](#)]
37. Zhang, J.E.; Xiao, W.J.; Luo, J.; Chen, Y.C.; Windley, B.F.; Song, D.F.; Han, C.M.; Safonova, I. Collision of the Tacheng block with the Mayile-Barleik-Tangbale accretionary complex in western Junggar, NW China: Implication for early middle Paleozoic architecture of the western Altai. *J. Asian Earth Sci.* **2018**, *159*, 259–278. [[CrossRef](#)]
38. Zheng, B.; Han, B.F.; Liu, B.; Wang, Z.Z. Ediacaran to paleozoic magmatism in west Junggar orogenic belt, NW China, and implications for evolution of central Asian orogenic belt. *Lithos* **2019**, *338–339*, 111–127. [[CrossRef](#)]
39. Yin, J.Y.; Chen, W.; Yuan, C.; Yu, S.; Xiao, W.J.; Long, X.P.; Li, J.; Sun, J.B. Petrogenesis of early Carboniferous adakitic dikes, Sawur region, northern West Junggar, NW China: Implications for geodynamic evolution. *Gondwana Res.* **2015**, *27*, 1630–1645. [[CrossRef](#)]
40. Yin, J.Y.; Chen, W.; Xiao, W.J.; Yuan, C.; Windley, B.F.; Yu, S.; Cai, K.D. Late Silurian-early Devonian adakitic granodiorite, A-type and I-type granites in NW Junggar, NW China: Partial melting of mafic lower crust and implications for slab roll-back. *Gondwana Res.* **2017**, *43*, 55–73. [[CrossRef](#)]
41. Zhang, C.; Santosh, M.; Liu, L.F.; Luo, Q.; Zhang, X.; Liu, D.D. Early Silurian to Early Carboniferous ridge subduction in NW Junggar: Evidence from geochronological, geochemical, and Sr-Nd-Hf isotopic data on alkali granites and adakites. *Lithos* **2017**, *300–301*, 314–329. [[CrossRef](#)]
42. Zheng, R.G.; Zhao, L.; Yang, Y.Q. Geochronology, geochemistry and tectonic implications of a new ophiolitic mélangé in the northern West Junggar, NW China. *Gondwana Res.* **2019**, *74*, 237–250. [[CrossRef](#)]
43. Ren, R.; Han, B.; Guan, S.; Liu, B.; Wang, Z. Linking the southern West Junggar terrane to the Yili block: Insights from the oldest accretionary complexes in west Junggar, NW China. *J. Asian Earth Sci.* **2018**, *159*, 279–293. [[CrossRef](#)]
44. Zhao, L.; He, G.Q. Geochronology and geochemistry of the Cambrian (~518 Ma) Chagantaolegai ophiolite in northern West Junggar (NW China): Constraints on spatiotemporal characteristics of the Chingiz-Tarbagatai megazone. *Int. Geol. Rev.* **2014**, *56*, 1181–1196. [[CrossRef](#)]
45. Han, B.F.; Ji, J.Q.; Song, B.; Chen, L.H.; Zhang, L. Late Paleozoic vertical growth of continental crust around the Junggar Basin, Xinjiang, China (Part I): Timing of post-collisional plutonism. *Acta Petrol. Sin.* **2006**, *22*, 1077–1086, (In Chinese with English Abstract).
46. Geng, H.Y.; Sun, M.; Yuan, C.; Xiao, W.J.; Xian, W.S.; Zhao, G.C.; Zhang, L.F.; Wong, K.N.; Wu, F.Y. Geochemical, Sr-Nd and zircon U-Pb-Hf isotopic studies of Late Carboniferous magmatism in the West Junggar, Xinjiang: Implications for ridge subduction? *Chem. Geol.* **2009**, *266*, 373–398. [[CrossRef](#)]
47. Gao, R.; Xiao, L.; Pirajno, F.; Wang, G.C.; He, X.X.; Yang, G.; Yan, S.W. Carboniferous-Permian extensive magmatism in the West Junggar, Xinjiang, north-western China: Its geochemistry, geochronology, and petrogenesis. *Lithos* **2014**, *204*, 125–143. [[CrossRef](#)]
48. Zong, R.W.; Fan, R.Y.; Gong, Y.M. Advances in the research on Carboniferous deep-water marine deposits in western Junggar, northwestern China. *Geol. J.* **2015**, *50*, 111–121. [[CrossRef](#)]
49. Qiu, T.; Zhu, Y.F. Geology and geochemistry of listwaenite-related gold mineralization in the Sayi gold deposit, Xinjiang, NW China. *Ore Geol. Rev.* **2015**, *70*, 61–79. [[CrossRef](#)]
50. Zhu, Q.; Zhu, Y. Chromitite genesis based on chrome-spinels and their inclusions in the Sartohay podiform chromitites in west Junggar of northwest China. *Ore Geol. Rev.* **2020**, *119*, 103401. [[CrossRef](#)]
51. Liu, Y.S.; Hu, Z.C.; Gao, S.; Günther, D.; Xu, J.; Gao, C.G.; Chen, H.H. In situ analysis of major and trace elements of anhydrous minerals by LA-ICP-MS without applying an internal standard. *Chem. Geol.* **2008**, *257*, 34–43. [[CrossRef](#)]
52. Sun, S.S.; McDonough, W.F. Chemical and isotopic systematics of oceanic basalt: Implications for mantle compositions and processes. *Geol. Soc. Lond. Spec. Publ.* **1989**, *42*, 313–345. [[CrossRef](#)]
53. Grant, J.A. The Isocon diagram: A simple solution to Gresens' equation for metasomatic alteration. *Econ. Geol.* **1986**, *81*, 1976–1982. [[CrossRef](#)]
54. Pearce, J.A. Statistical analysis of major element patterns in basalts. *J. Petrol.* **1976**, *17*, 15–43. [[CrossRef](#)]
55. Winchester, J.A.; Floyd, P.A. Geochemical discrimination of different magma series and their differentiation products using immobile elements. *Chem. Geol.* **1977**, *20*, 325–343. [[CrossRef](#)]
56. Cabanis, B.; Lecolle, M. Le diagramme La/10-Y/15-Nb/8: Un outil pour la discrimination des series volcaniques et la mise en evidence des processys de mélange et/ou de contamination crustale. *Comptes Rendus Acad. Sci. II* **1989**, *309*, 2023–2029.
57. Pearce, J.A. Geochemical fingerprinting of oceanic basalts with applications to ophiolite classification and the search for Archean oceanic crust. *Lithos* **2008**, *100*, 14–48. [[CrossRef](#)]
58. Shervais, J.W. Ti-V plots and the petrogenesis of modern and ophiolitic lavas. *Earth Planet. Sci. Lett.* **1982**, *59*, 101–118. [[CrossRef](#)]
59. Dilek, Y.; Furnes, H. Ophiolite genesis and global tectonics: Geochemical and tectonic fingerprinting of ancient oceanic lithosphere. *Geol. Soc. Am. Bull.* **2011**, *123*, 387–411. [[CrossRef](#)]
60. Pearce, J.A. Immobile element fingerprinting of ophiolites. *Elements* **2014**, *10*, 101–108. [[CrossRef](#)]
61. Karkalis, C.; Magganas, A.; Koutsovitis, P.; Pomonis, P.; Ntaflos, T. Multiple rodingitization stages in alkaline, tholeiitic, and calc-alkaline basaltic dikes intruding exhumed serpentized Tethyan mantle from Evia Island, Greece. *Lithosphere* **2022**, *2022*, 9507697. [[CrossRef](#)]
62. Bach, W.; Jöns, N.; Klein, F. Metasomatism within the ocean crust. In *Metasomatism and Chemical Transformation of Rocks: The Role of Fluids in Terrestrial and Extraterrestrial Processes*; Lecture Notes in Earth Systems Sciences; Harlov, D., Austrheim, H., Eds.; Springer: Berlin/Heidelberg, Germany, 2013; pp. 253–288.

63. Coleman, R.G. Low-temperature reaction zones and alpine ultramafic rocks of California Oregon and Washington. *U.S. Geol. Surv. Bull.* **1967**, *1247*, 1–49.
64. Hatzipanagiotou, K.; Tsikouras, B.; Migiros, G.; Gartzos, E.; Serelis, K. Origin of rodingites in ultramafic rocks from Lesvos Island (NE Aegean, Greece). *Ophioliti* **2003**, *28*, 13–23.
65. Frost, B.R.; Beard, J.S. On silica activity and serpentinization. *J. Petrol.* **2007**, *48*, 1351–1368. [[CrossRef](#)]
66. Pomonis, P.; Tsikouras, B.; Karipi, S.; Hatzipanagiotou, K. Rodingite formation in ultramafic rocks from the Koziakas ophiolite, western Thessaly, Greece: Conditions of metasomatic alteration, geochemical exchanges and T-X(CO) evolutionary path. *Can. Mineral.* **2008**, *46*, 569–581. [[CrossRef](#)]
67. Tsikouras, B.; Karipi, S.; Hatzipanagiotou, K. Evolution of rodingites along stratigraphic depth in the Iti and Kallidromon ophiolites (Central Greece). *Lithos* **2013**, *175*, 16–29. [[CrossRef](#)]
68. Qiu, T.; Zhu, Y.F. Listwaenite in the Sartohay ophiolitic mélange (Xinjiang, China): A genetic model based on petrology, U-Pb chronology and trace element geochemistry. *Lithos* **2018**, *302–303*, 427–446. [[CrossRef](#)]
69. Li, D.; He, D.F.; Qi, X.F.; Zhang, N.N. How was the Carboniferous Balkhash-West Junggar remnant ocean filled and closed? Insights from the well Tacan-1 strata in the Tacheng basin, NW China. *Gondwana Res.* **2015**, *27*, 342–362. [[CrossRef](#)]